Chemical Engineering Journal 495 (2024) 153080

Contents lists available at ScienceDirect

Chemical Engineering Journal

journal homepage: www.elsevier.com/locate/cej

Core–Shell catalyst particles for tandem catalysis: An experimental/numerical approach towards optimal design

Najmeh Bashiri [a,b], Georg Brösigke [c,*], Esteban Gioria [b,e], Johannes Schmidt [b], Martin Konrad [e], Rafael L. Oliveira [g,h], Michael Geske [e], Frank Rosowski [e,f], Sebastian Matera [d], Reinhard Schomäcker [a], Arne Thomas [b], Jens-Uwe Repke [c]

[a] Department of Chemistry, Technical Chemistry, Technische Universität Berlin, Straße des 17. Juni 124, 10623 Berlin, Germany
[b] Department of Chemistry, Functional Materials, Technische Universität Berlin, Straße des 17. Juni 124, 10623 Berlin, Germany
[c] Process Dynamics and Operations Group, Technische Universität Berlin, Straße des 17. Juni 135, 10623 Berlin, Germany
[d] Theory Department, Fritz Haber Institute of the Max Planck Society, Faradayweg 4-6, 14195 Berlin, Germany
[e] BasCat - UniCat BASF JointLab, Technische Universität Berlin, Str. des 17. Juni 124, 10623 Berlin, Germany
[f] BASF SE, Catalysis Research, Carl-Bosch-Str. 38, 67056 Ludwigshafen, Germany
[g] Institute of the Low Temperature and Structure Research of the Polish Academy of Sciences, Str. Okolna 2, 50-422, Wroclaw, Poland
[h] Chemistry Department of Federal University of Pernambuco, Av. Jorn. Anibal Fernandes, 50740-560, Recife-PE, Brazil

ARTICLE INFO

Keywords:
Core–Shell
Tandem catalysis
RWGS
FTS
Optimal design

ABSTRACT

Tandem catalysis is a promising approach to intensify chemical processes and increase their efficiency. On the other hand, the design of efficient, optimal and targeted tailored tandem catalysts is yet so challenging as the optimal catalyst loading is difficult to assess a priori. In this article, we present a concise route towards the design of optimal core–shell tandem catalyst particles on the example of coupled RWGS and FTS reactions for any specific spherical morphology. The route features five consecutive steps including: tandem system identification, catalyst synthesis, i.e. mono- and tandem-functional, catalyst characterization and initial performance test, kinetic modeling with parameter estimation if necessary, and optimal design of catalysts. The initial step features thermodynamic equilibrium calculations for RWGS and FTS showing a common operational window. Then, Pt and Co are selected as active metals and the formulation of the tandem catalyst is designed. For the second step, the synthesis route for the tandem catalyst Pt,CeO_2@SiO_2-Co, and the mono-functional catalysts, Pt@SiO_2 and CeO_2@SiO_2-Co are presented. For the third step, all catalysts were tested for CO_2 hydrogenation as an exemplary tandem process. A reduced transport model from literature was adjusted for RWGS and FTS reactions with kinetic expression from literature to enable numerical optimization. The kinetic parameters are estimated based on the performance tests of the mono-functional reference materials, i.e. Pt@SiO_2 for RWGS and CeO_2@SiO_2-Co for FTS. The model is validated by cross comparison to the data from the tandem reaction setup. In the fifth step, the model was used for the numerical optimization of the catalyst loading on core and shell leading to the identification of the optimal design, resulting in a significant increase of C2+ Yield.

1. Introduction

Tandem and multi-component reactions involve combining multiple consecutive reactions into a single reactor [1,2]. This offers various advantages compared to the traditional sequential reactions, including the elimination of process steps like separation, purification, and intermediate transfer which leads to cost savings and a more eco-friendly process [3,4]. The tandem approach has been used extensively in organic synthesis and recently in chemical processes such as CO and CO_2 hydrogenation and alcohol oxidation [5–9]. Highlighting CO_2 as a prominent greenhouse gas, the concept of utilizing it as a carbon feedstock for the production of carbon based chemicals has attracted considerable attention and noticed as an alternative to conventional non-renewable petrochemical sources.

The key to the tandem approach is the ability to generate intermediates and convert them into complex products in one pot, requiring at least two active phases in the reaction space for sequential reactions [10]. Despite the significant developments recently achieved

* Corresponding author.
E-mail addresses: n.bashiri@campus.tu-berlin.de (N. Bashiri), georg.broesigke@tu-berlin.de (G. Brösigke).

https://doi.org/10.1016/j.cej.2024.153080
Received 15 April 2024; Received in revised form 7 June 2024; Accepted 11 June 2024
Available online 13 June 2024

Nomenclature

Abbreviations	
GHSV	Gas Hourly Space Velocity, nmL g^{-1} h^{-1}
RWGS	Reverse Water Gas Shift
FTS	Fischer–Tropsch Synthesis
NLP	Nonlinear programming (problem)
NPs	Nano Particles
Greek Symbols	
δ	Distance between core surface and shell surface, nm
ε	Porosity, –
γ	Tortuosity, –
κ	Thermal conductivity, W m^{-1} K^{-1}
ρ	Density, kg m^{-3}
Latin Symbols	
A	Catalyst loading, g m^{-2}
c	Molar concentration, mol L^{-1}
d	Diameter, nm
f	Objective function
g	Nonlinear constraints
k	Pre-exponential factors
m	Mass, mg
n	Number of particles, –
N	Number species, –
p	Pressure, bar
R^P	Pore radius, Å
R_{shell}	Radial coordinate of Shell, m
r	Radial coordinate, m
T	Temperature, °C
v^P	Pore volume, cm g^{-3}
x	Molar fraction, mol %
y	Mass fraction, wt.%
Y_P	Yield of product, %
z	Unknown variables
Indices	
i	Specie
l	Reaction
Subscripts	
0	Nominal operating point

in this field, one-pot catalytic processes still have no common application due to the complexity of identifying and controlling active phases in multi-site catalysts [11,12]. One strategy to simplify the intricate interactions between active phases in multi-site catalysts to systematically comprehend tandem processes, is employing core–shell structures that provide a series of well-optimized isolated active sites. The core–shell structures can guarantee the close distance between the active sites [13]. Furthermore, the compatibility of two active phases can be optimized by controlling the structural properties, including the shape, quantity, and size of active metals, as well as the specific distance between them, the pore size distribution, and the porosity of the shell [14,15]. Although, using a shell may block fraction of the active surface of the core, covering and encapsulating the nanoparticles (NPs) serves as a protective measure against issues such as aggregation, leaching, and sintering. Additionally, a high porous shell can provide efficient mass transfer within the core–shell catalyst [16–18].

The synthesis of bimetallic core–shell NPs with controllable structure is challenging and demands the development of precise model systems in the planning of multi-step synthesis. Su et al. [19] proposed a four-step method to synthesize 85 nm CeO_2-Pt@SiO_2 core–shell structures. The process included hydrothermal synthesis of CeO_2 using high molecular weight PVP as a capping ligand, pre-synthesis of Pt NPs as the initial active metal on the core, hydrothermal deposition of Pt NPs on the CeO_2, and sol–gel synthesis of the silica shell. Despite the successful development of a well-defined catalyst, challenges in scaling up can persist due to the demanding conditions imposed by the use of high molecular weight PVP and the small size of nanoparticles, particularly in steps 1 and 3 of their proposed synthesis method. Building on this method, Xie et al. [20] extended the network by integrating homogeneous cobalt NPs onto the shell through two additional synthesis steps, resulting multi active phases catalyst within a total of six synthesis steps. This structure functioned as a tandem catalyst for CO_2 hydrogenation, achieving approximately 10% and 40% selectivity towards C_2+ in hydrocarbon distribution at 350 °C and 250 °C, respectively. In a recent study, Gioria et al. [21] introduced a distinctive morphology for the Pt-SiO_2@SiO_2-Co catalyst, simplifying the rational synthesis method into five steps. This involved replacing CeO_2 NPs with SiO_2 in the core and performing an in-situ synthesis of Pt NPs on the core instead of using pre-synthesized Pt. The resulting structure comprised a 199 nm silica core covered by a 50 nm-thick mesoporous silica shell, exhibiting a 14% selectivity toward C_2+ and 86% methane in total hydrocarbon distribution in CO_2 hydrogenation.

In both studies, CO_2 hydrogenation followed the carbon monoxide intermediate pathway through two sequential reactions. Initially, CO_2 is transformed into CO via RWGS (Reverse Water Gas Shift) occurring on the core. Subsequently, as produced CO diffuses through the porous shell and reacts on its surface, hydrocarbons are generated via the FTS (Fischer–Tropsch Synthesis). Pt NPs which are well known as an active phase for RWGS at low temperatures are located on the core and Co NPs which activate both CO and CO_2 are located on the Shell [22–24]. While well-designed tandem catalysts have been employed above, their performance in tandem systems is currently restricted, exhibiting 60% selectivity for CO and predominantly yielding methane in hydrocarbon products. The optimum performance of such systems concerning catalyst structure remains unclear.

The core of the rational catalyst design for a tandem process lies in understanding the relation between catalyst structure, properties, and performance. What constitutes an efficient strategy for optimizing the tandem catalyst's structure? The conventional approach involves the energy- and time-intensive process of experimentally determining the optimal ratio of various parameters such as shell thickness, porosity, and the ratio of active metal, through a multi-step core–shell synthesis and performance tests. In this article, we propose a new, 5 steps protocol to design an optimal core–shell catalyst design considering the structural-performance relationship. The aim is not to present the best performing core–shell structure catalyst for one certain reaction network but line out a blueprint for the proper design of any of such systems within its limits. The initial step entails investigating of a tandem reaction through thermodynamic simulation. Subsequently, the approach involves the following steps: designing a controllable core–shell structure, conducting characterization and systematic catalytic performance tests including both mono- tandem function catalysts, formulating and validating a mathematical model for the system and applying the validated model for numerical optimization of the catalyst's properties. The final step of synthesizing the catalyst again for optimized catalyst properties was not part of the study.

To show the possibility of a CO_2 hydrogenation tandem process through sequential RWGS and FTS reactions, as well as to create a comparable model catalyst with previous reports, Pt NPs and Co NPs were chosen to facilitate RWGS and FTS reactions, respectively. A general and rational synthesis method based on the microemulsion approach is introduced for creating a unique multi-core@shell structure. This structure features a well-defined architecture of Pt and Co active metals within a mesoporous silica shell, ensuring the rather constant values of each individual active metal for mono- tandem function catalysts. Importantly, given the precious nature of Pt, the model catalysts have been designed using a significantly lower proportion of Pt compared to Co. Successfully, the optimal catalyst formulation regarding the active metals loading is achieved through numerical optimization based on the approach outlined.

2. Methodology

2.1. Materials and chemicals

Chemicals including cerium nitrate hexahydrate ($Ce(NO_3)_3.6H_2O$, 99%, Acros Organics), potassium tetrachloroplatinate (II) (K_2PtCl_4, 98%, abcr), cobalt carbonyl ($Co_2(CO)_8$, Sigma-Aldrich), polyvinylpyrrolidone (PVP, M_w = 29 000, Sigma-Aldrich), tetradecyltrimethylammonium bromide (TTAB, Alfa Aesar), Cetyltrimethylammonium bromide (CTAB, >98%, Roth), oleic acid (Simgma-Aldrich), tetraethyl orthosilicate (TEOS, Sigma-Aldrich), ammonia (25%, Sigma-Aldrich) and ammonium nitrate (NH_4NO_3, Sigma-Aldrich) were used for the synthesis of nanoparticles. Ethyl acetate (≥99.5%, Roth), ethylene glycol (Sigma-Aldrich), chloroform (≥99%, Roth), toluene (≥99.5%, Roth), hexane (≥99%, Roth) and 1,2- dichlorobenzene (98%, Acros Organics) were applied as solvents during synthesis. Deionized water was supplied from a Millipore Elix 20 set up for all experiments. Chemicals were utilized without further purification.

2.2. Synthesis of the nanoparticles

2.2.1. Synthesis of oleic acid-capped CeO_2 NPs

CeO_2 NPs have been prepared through a shape and size-controlled rational approach in one-pot hydrothermal method described in [25] with some modifications. Initially, 24.41 mmol of $Ce(NO_3)_3.6H_2O$ were dissolved in 15 mL of deionized water. Then, an aqueous solution of cerium along with 15 mL of toluene, 632 μL of oleic acid, and 150 μL of tert-butylamine were respectively added to a 50 mL teflon chamber without stirring. The autoclave reactor was heated to 180 °C and remained for 24 h. After reaction, possible impurities were removed by centrifuging the product at 4000 rpm for 15 min. Oleic acid-capped CeO_2 NPs were precipitated by adding 40 mL ethanol to the obtained brown organic phase and separated by centrifugation at 4000 rpm for 15 min. The purified CeO_2 NPs can be dispersed in any non-polar solvents and used as an organic phase for micro-emulsion synthesis. Here, CeO_2 NPs were rapidly dispersed in 1 mL of chloroform using 2 min sonication and applied in the following step of the synthesis.

2.2.2. Synthesis of PVP and TTAB-capped Pt NPs

PVP and TTAB-capped Pt NPs were synthesized through the alcohol reduction method proposed by Tsung et al. [26], with some modification. Briefly, 0.0219 mmol of K_2PtCl_4 were dissolved in 4 mL ethylene glycol using sonication. The Pt(II) solution was injected into a schlenk flask containing 0.109 mmol of TTAB and 0.196 mmol of PVP (M_w = 29 000) dissolved in 10 mL ethylene glycol under argon protection. The alcoholic solution was stirred at 250 rpm for 15 min at ambient temperature. The reaction temperature was then increased to 175 °C and the reaction continued for 30 min at this condition. The formation of Pt NPs was indicated by a black color of the mixture above 120 °C. After natural cool down, 60 mL of acetone were added to precipitate the PVP and TTAB-capped Pt NPs. The pre-synthesized NPs were collected by centrifugation at 6000 rpm for 5 min, and then immediately dispersed in 1 mL chloroform for the subsequent synthesis step.

2.2.3. Synthesis of oleic acid-capped Co NPs

The mono-dispersed Co NPs were obtained from the thermal decomposition of cobalt carbonyl under inert conditions [21]. 290 μL of oleic acid were dissolved in 30 mL of o-dichlorobenzene in a three-neck flask equipped with a condenser and heated up to 170 °C. Subsequently, 2.93 mmol of $Co_2(CO)_8$ dissolved in 6 mL of o-dichlorobenzene was quickly injected into the flask, causing a dark-reddish color of the solution and instantly releasing CO due to the thermal decomposition of cobalt carbonyl. The reaction was continued for 20 min, and cooled to the ambient temperature naturally. Eventually, the Co NPs were precipitated using 2-propanol, recovered by centrifugation at 9000 rpm for 30 min, and redispersed in 60 mL hexane.

2.2.4. Synthesis of CeO_2@SiO_2 as inert core–shell catalyst

To synthesize a mesoporous silica shell, an oil-in-water micro-emulsion technique, inspired from magnetic core–shell NPs [27], was applied. To prepare the water-surfactant phase, 1.09 mmol of CTAB were dissolved in 20 mL deionized water. Then, 1 mL chloroform as organic phase, containing the stabilized pre-synthesized core, was gradually added into the aqueous solution and vigorously mixed for 20 min until a milky homogeneous oil/water solution was achieved. This solution was then heated up to 60 °C for 20 min to facilitate the evaporation and removal of chloroform. Subsequently, the resulting mixture was diluted using 80 mL of deionized water, followed by sequential additions of 6 mL of ammonia solution, 1 mL of TEOS, and 10 mL of ethyl acetate for shell formation. The solution was sonicated for 30 s and the reaction was slowly stirred for 6 h at 40 °C. Afterward, the product was separated from the light yellow suspension with centrifugation at 4000 rpm for 15 min and washed five times using deionized water and ethanol. To remove CTAB, the product was mixed with 200 mL of 10 mg mL^{-1} ammonium nitrate solution for 6 h at ambient temperature. Finally, CeO_2@SiO_2 NPs were washed several times with ethanol and deionized water.

2.2.5. Synthesis of Pt@SiO_2 as RWGS core–shell catalyst

Pt@SiO_2 core–shell NPs were obtained using the synthesis method described in Section 2.2.4. Pre-synthesized Pt NPs dissolved in 1 mL chloroform were mixed with 20 mL aqueous solution of 1.09 mmol CTAB under a stirring rate of 550 rpm for 20 min. The homogeneous light gray micro-emulsion was heated up to 60 °C for 20 min. Upon the removing of chloroform, 80 mL of deionized water, 6 mL of ammonia solution, 1 mL of TEOS, and 10 mL of ethyl acetate were added followed by sonication for 30 s. The reaction solution was stirred slowly at 40 °C for 6 h, and the product was isolated from the gray reaction suspension with centrifugation at 4000 rpm for 15 min. After being washed multiple times with ethanol and deionized water, CTAB was removed by mixing the resultant products with 200 mL ethanol containing 10 mg mL^{-1} of NH_4NO_3 for 6 h, and it was subjected to a final washing step.

2.2.6. Synthesis of CeO_2@SiO_2-Co as FTS core–shell catalyst

In this study, FTS core–shell catalyst was designed by utilizing the CeO_2@SiO_2 as an inert support and oleic acid-capped Co NPs as the active phase. The deposition of Co NPs onto the silica surface was carried out by preparing a dispersion of CeO_2@SiO_2 in hexane, followed by the addition of the desired quantity of Co NPs to the support. The mixture was vortexed for 15 min, and the solvent was evaporated and removed from the structure at ambient temperature. In the final step, the resulting dried catalyst was calcined at 350 °C for a duration of 2 h with a heating rate of 5 °C min^{-1} for removing any residual organic components.

2.2.7. Synthesis of Pt,CeO_2@SiO_2-Co as tandem catalyst

Pt,CeO_2@SiO_2-Co tandem catalyst was synthesized using a multi-step synthesis method. Initially, one batch of pre-synthesized Pt and CeO_2 NPs were prepared according to the method described in 2.2.1 and 2.2.2 sections. Next, Pt and CeO_2 NPs were separately dispersed in 500 μL of chloroform and added to 20 mL aqueous solution containing 1.09 mmol of CTAB. The solution was vigorously stirred to obtain homogeneous chloroform in water micro-emulsion solution. After the removal of chloroform at 60 °C, the solution was diluted with 80 mL of deionized water, 6 mL of ammonia solution, 1 mL of TEOS, and 10 mL of ethyl acetate. The resulting mixture was sonicated for 30 s and the shell synthesis was carried out at 40 °C for 6 h. The core–shell NPs were obtained by centrifugation and washed multiple times with deionized water and ethanol. To remove CTAB from the structure, the product was mixed with 10 mg mL^{-1} ammonium nitrate in 200 mL ethanol. After separating core–shell NPs, a final washing step was performed using deionized water and ethanol. The dried sample, named

$Pt,CeO_2@SiO_2$, was dispersed in hexane for the next synthesis step. To apply Co NPs as second active metal, onto the core–shell structure, a wetness impregnation was performed. A desired amount of Co NPs in hexane was added to the $Pt,CeO_2@SiO_2$ suspension and mixed for 15 min using a vortex. Hexane was then evaporated and removed from the structure at ambient temperature. Finally, the catalyst was calcined at 350 °C for 2 h with a heating rate of 5 °C min^{-1}.

2.3. Characterizations

The morphology, elemental distribution, size, and geometry of the pre-synthesized as well as core–shell NPs were investigated by transmission electron microscopy (TEM) and high-resolution scanning electron microscopy (STEM). The TEM analysis was conducted using a conventional TECNAI $G^2$20 S-TWIN with LaB6 emitter from FEI/TFS company operated at 200 kV. STEM imaging was performed with a probe cs-corrected JEM-ARM300F2 cold FEG from JEOL Ltd., Japan, operated at 300 kV. Also, the STEM images were recorded with a camera length of 8 cm, which corresponded to a high-angle annular dark field (HAADF) detection angle of 68–280 mrad. The microscope implemented in the mapping investigation was equipped with a dual SDD EDX system from JEOL Ltd., with an energy resolution of 134 eV and an angle of 2 × 2 sr.

Etching X-ray photoelectron spectroscopy (XPS) was performed to evaluate the composition of materials and the chemical state of the corresponding elements on the surface and inside the core–shell NPs. The measurements were performed using a ThermoScientific K-Alpha$^+$ X-ray Photoelectron Spectrometer. All samples were analyzed using a microfocused, monochromated Al Kα X-ray source (1486.68 eV; 400 micrometer spot size). The elemental spectra were fitted with an asymmetric voigt profile after the subtraction of a Shirley background using Avantage software. Due to the absence of an internal reference level and the difficulty in determining the sample work function, we utilized the C–C peak of the C1 spectra for adventitious carbon at 284.8 eV as a reference point [28]. All the spectra were adjusted in correspondence with the C–C component position at each level of etching.

Powder X-ray diffraction (XRD) was performed to study the crystalline phase of core–shell NPs using a Bruker D8 Advance diffractometer in reflection geometry. Before the test, NPs were ground on a silica sample holder, and a Cu Kα anode (λ = 1.54178 Å) with a current of 40 mA and a voltage of 40 kV was utilized for the collection of data.

To determine the surface area, pore size, and pore volume of core–shell NPs nitrogen sorption measurements were performed using QuadraSorb SI device Quantachrome Instruments, Boynton Beach, FL, USA, at a cryogenic temperature of 77 K. The NPs were dried and degassed at 200 °C for 12 h prior to the analysis. Brunauer-Emmett-Teller (BET) methods were applied to calculate the surface areas over a pressure range of 0.05–0.1 = p/p_0 using the N_2 adsorption isotherms and the linear fit was obtained using 5 points in the pressure range of 0.04–0.25. Furthermore, the surface area obtained was calculated using the BETSI tool for comparison and obtaining more precise results. To calculate the pore size distributions, Non-Local Density Functional Theory (NLDFT) in equilibrium mode on carbon was utilized for N_2 sorption data collected at 77 K. CO_2 sorption isotherms were recorded using the same device at room temperature.

The elemental weight loading (wt%) was quantified through the inductively coupled plasma (ICP) measurement using a Horiba Scientific ICP Ultima 2 device (Horiba, Kyoto, Japan). To prepare the samples for ICP, they were dispersed in 2 mL of HF and 5 mL of HNO_3 and heated at 200 °C for 5 h using an autoclave reactor. This digestion process was carried out to destroy the samples into their constituent elements for further analysis.

Table 1
Catalyst properties in each reactor.

Reactor No.	Catalyst name	m mg	y_{Pt} wt.%	y_{Co} wt.%	v^P cm g^{-3}	R^P Å	δ nm	d nm
1	$Pt@SiO_2$	45.8	0.54	0.0	0.352	8.068	55.1	117.1
2	$Pt,CeO_2@SiO_2$-Co	50.5	0.50	3.8	0.229	13.845	69.3	205.1
3	$CeO_2@SiO_2$-Co	51.9	0.00	4.7	0.364	18.97	39.5	90.9
4	$CeO_2@SiO_2$	48.1	0.00	0.0	0.381	18.14	39.5	90.9

2.4. Catalytic performance test

The catalytic performance tests were conducted in five tubular parallel reactors. Four reactors were loaded in order with $Pt@SiO_2$ (RWGS) in R1, $Pt,CeO_2@SiO_2$-Co (tandem) in R2, $CeO_2@SiO_2$-Co (FTS) in R3, and $CeO_2@SiO_2$ (inert) in R4 while the fifth reactor was dedicated to bypass measurement, Fig. S.1 [29]. Catalyst particles with the sieve fraction of 100–200 μm diluted with davisil at the same size range were used for the catalytic testing. The properties of catalysts loaded in four reactors are presented in Table 1. Each reactor has a length of 64.5 cm, an inner diameter of 9.4 mm, and an effective diameter of 6.4 mm, and a reactor head containing inlet connections for the feed and a hull for placing the thermocouple with an outer diameter of 3 mm. The electric furnace was used to supply the heat and the temperature was monitored at three local points along the length of the reactor while the catalyst bed was positioned in the isothermal zone. The flows of the feed stream, including N_2, Ar, H_2, and CO_2, were regulated using individual mass flow controllers (MFCs) for each component.

Prior to the reaction, all catalysts were in situ reduced by 50% of H_2 and 50% N_2 flow with GHSV of 30 000 nmL g^{-1} h^{-1}, at 350 °C and atmospheric pressure for 2 h. Then, the gas composition and temperature switched to the experimental design which is summarized in Table S.1 [29], and the pressure of 10 bar was built up according to each operation condition. The reactions were performed for the duration of 12 h under each operational condition, and data was recorded using an online gas chromatograph (GC, Agilent 7890B) at 3 h intervals. The exit gas stream was diluted with N_2 and led through a multi-position valve to the GC for analysis. To prevent condensation of the effluent, the outlet stream was transferred with heated lines at 180 °C to the GC. Helium was used as the GC carrier gas, while Ar served as the internal standard during all the experiments. The GC was equipped with a thermal conductivity detector (TCD) and a flame-ionized detector (FID) for the quantification of non-carbon and carbon base components, respectively. To separate, H_2, N_2, and Ar, an HP-Plot 5A column (30 m × 0.53 mm × 50 μm) was utilized, and carbon-containing components were separated using an HP-Plot Q column (30 m × 0.53 mm × 40 μm) from Agilent with a Polyarc® reactor placed prior to FID.

2.5. Modeling

As building a valid model is crucial for the 5th step of the proposed design protocol, the modeling methodology is briefly lined out here. For modeling the catalyst performance, the fast computing model for core–shell tandem catalyst particles proposed in [30] is used and adjusted for the present system of RWGS and FTS. The model is based on first principles conservation laws for mass and energy and calculates the concentration profiles of all involved gas phase species as well as the temperature profile within n core–shell catalyst particles in a reactor. The diffusive fluxes within the particle are modeled with Knudsen diffusion. All physical properties of the catalyst, like void fraction, the amount of active metal or pore diameter are direct input parameter to the model. For a detailed description of the model please be referred to the original literature source. For model formulation, MOSAICModeling [31,32] is used. The generated code is then exported and solved in MATLAB®, where the nonlinear solver fsolve with the trust-region-dogleg algorithm is used. The kinetics for RWGS on the

Table 2
Transport parameters for simulation study.

Name	Parameter	Value	Unit
κ	Thermal conductivity	1.2	$W\,m^{-1}\,K^{-1}$
γ	Tortuosity	1.5	–

core were taken from [33] and for FTS on the shell the kinetics from [34] were applied up to a chain length of C4 resulting in 16 gas phase species in the model (N_2, H_2, H_2O, CO, CO_2, CH_4, CH_3OH, C_2H_4, C_2H_6, C_2H_5OH, C_3H_6, C_3H_8, C_3H_7OH, C_4H_8, C_4H_{10} and C_4H_9OH). The considered reactions in kinetic models are depicted in Table S.2. As conversion of CO_2 on the CeO_2@SiO_2-Co catalyst in reactor 3 could be observed contrary to the inert one in reactor 4, it was concluded that the Co was active for RWGS by itself. Therefore, the kinetics from [33] were also used to account for RWGS on the shell, assuming the same mechanism but using different pre-exponential factors for core and shell. Moreover, as no production of alcohols was observed in the experiments, their production rates were set to 0 in the model. The catalyst structure used in this study differs from the original sources of the kinetic expressions in terms of structure and support. Nevertheless, the kinetics from [33] was developed on a system most similar to the one used in this study. The catalyst used in [34] used the same active metal supported on a different compound (i.e. active carbon). On the other hand, the proposed kinetics were the most detailed ones utilizing at least the same active metal. In order to adapt the kinetic expressions to the system used here, the pre-exponential parameters of the kinetic expressions were estimated again based on the mono-functional catalytic performance experiments described in Section 2.4. This approach implies the assumption that the tandem system can be described by superpositioning the mono-functional reaction rates.

As the model requires a number n of core–shell catalyst particles to be provided as well as a catalyst loading A and a porosity ε these numbers were calculated from a nonlinear equation system added to the model described in [30].

$$\rho^{part} = \frac{1}{y_{Pt}/\rho_{Pt} + y_{Co}/\rho_{Co} + (y_{inert})/\rho_{inert}} \tag{1}$$

$$m^{\text{part}} = \frac{\pi \cdot 4/3 \cdot (R_{\text{shell}})^3}{\frac{1}{\rho^{\text{part}}} + v^{\text{P}}} \tag{2}$$

$$\varepsilon = \frac{v^{\text{P}} \cdot m^{\text{part}}}{\pi \cdot 4/3 \cdot (R_{\text{shell}})^3} \tag{3}$$

$$n = \frac{m^{\text{overall}}}{m^{\text{part}}} \tag{4}$$

$$A_{l,r} = y_{l,r} \cdot \frac{m^{\text{part}}}{4 \cdot \pi \cdot (r)^2} \tag{5}$$

The overall catalyst mass m^{overall}, the pore volume v^{P} and the weight percentage of the active metals y were taken from the characterization results. The transport propoerties are listed in Table 2.

2.6. Parameter estimation

The pre-exponential parameter of the RWGS on the Pt-core was estimated based on the experimental results of the mono functional catalyst Pt@SiO_2. The pre-exponential parameters for the FTS and RWGS on the Co-shell were estimated based on the experimental results of the mono-functional catalyst CeO_2@SiO_2-Co. The results of the tandem catalyst Pt,CeO_2@SiO_2-Co can therefore be used as cross validation as their information is not utilized during the parameter estimation. Experiment numbers 1 & 2 from Table S.1 were omitted as steady state was not reached. For the parameter estimation, an optimization problem is formulated:

$$\min_k \quad f(z,k) = \sum_i^N \left(\frac{x_i^{\text{exp.}} - x_i^{\text{sim.}}}{x_i^{\text{exp.}}} \right)^2 \tag{6}$$

$$\text{subject to:} \quad g(z,k) = 0 \tag{7}$$

to find the best set of parameters k minimizing the deviation of measured molar fraction $x_i^{\text{exp.}}$ (mean of 4 measurements on the same set-point) and simulated molar fraction $x_i^{\text{sim.}}$ of all N components in the objective function f. The nonlinear constraints g include the core–shell model described in Section 2.5. The deviation is weighted by the measured value to normalize the contribution of all measurements, as they are of different order of magnitude. For the Pt-core CO, CO_2, and H_2 concentrations were used, and for the Co-shell CO, CO_2, CH_4, C_2H_6 and H_2 were considered. As no C_3H_8 was detected in the catalytic performance test of the mono-functional CeO_2@SiO_2-Co catalyst, this specie was not included in the parameter estimation.

For the estimation, a bootstrapping approach [35] was chosen with a total of 300 dice rolls for each estimation and the standard deviation for the concentrations from the experiments was used to weigh the objective function. The parameter estimation was carried out in MATLAB® via the lsqnonlin function. The estimated results and the initial values from the original literature sources are displayed in Table 3. All parameters except for $k_{7,0}$ could be identified as the std. deviation indicates. The parameter $k_{7,0}$ is the pre-exponential factor for the generation of alkanes.

2.7. Numerical optimization

For the optimization of the catalyst design several decision variables could be chosen, such as catalyst loading, porosity or shell thickness. Here, catalyst loading was chosen as it could be aimed for very precisely in the synthesis. MOSAICmodeling [36] was used to generate code for AMPL [37], where the optimization algorithm ipopt [38] is utilized. The optimization problem is stated as follows:

$$\min_A \quad f(z,A) = 1 - Y_{C_{2+}} \tag{8}$$

$$\text{subject to:} \quad g(z,A) = 0 \tag{9}$$

$$y_{\text{inert}} \geq \in [0.95, 0.90] \tag{10}$$

with f being the objective function to minimize (i.e. maximize the Yield of C_{2+} components $Y_{C_{2+}}$), A being the catalyst loading, g being the core–shell model representing the nonlinear constraints, and z the unknowns from the core–shell model i.e., concentrations, temperature, etc. The mass fraction of the inert support y_{inert} is bounded to a certain minimum threshold of (a) 95% and (b) 90%. This threshold might vary from case to case but needs to be specified as otherwise the mathematical model would converge to a point where the catalyst particle consists of 100% active material and no inert material, such as support. Another approach would be to use cost functions for the reaction products and the catalyst material, which is beyond the scope of this article.

3. Results

3.1. Characterization of core–shell catalysts

A general and rational synthesis method based on the microemulsion approach is introduced for creating a unique multi-core–shell structure with a well-defined architecture of Pt and Co as active metals. Fig. 1 illustrates the stepwise synthesis of multi-core–shell catalysts. For the RWGS catalyst, Pt@SiO_2, the process involves two main synthesis steps: (1) the synthesis of TTAB and PVP-capped Pt NPs and (2) the subsequent formation of the silica shell. The FTS, CeO_2@SiO_2-Co, and tandem, Pt,CeO_2@SiO_2-Co, catalysts, on the other hand, follow four distinct steps: (1) the synthesis of the oleic acid capped-ceria and TTAB and PVP-capped Pt NPs as core, (2) the shell formation, (3) the synthesis of oleic acid-capped Co NPs, and (4) the deposition of Co NPs onto the silica surface. Pt NPs serve as the active metal in the core for both the RWGS and tandem catalysts, while CeO_2 NPs is employed as

Table 3
Kinetic parameter values.

Catalyst	Reaction	Parameter	orig. val	est. val	std. dev	Unit
Pt	RWGS	$N_S K_3 * k_4$	5.7×10^{10} [33]	1.6517×10^{12}	4.7413×10^{11}	mol kg^{-1} s
Co	RWGS	$N_S K_3 * k_4$	5.7×10^{10} [33]	2.8275×10^{11}	4.4817×10^{10}	mol kg^{-1} s
Co	FTS	$k_{3,0}$	1.85×10^{7} [34]	1.1248×10^{9}	3.9395×10^{8}	mol kg^{-1} s
Co	FTS	$k_{7,1,0}$	8.01×10^{7} [34]	4.3205×10^{9}	4.5644×10^{9}	mol kg^{-1} s
Co	FTS	$k_{7,0}$	3.22×10^{7} [34]	6.7461×10^{10}	2.2047×10^{11}	mol kg^{-1} s

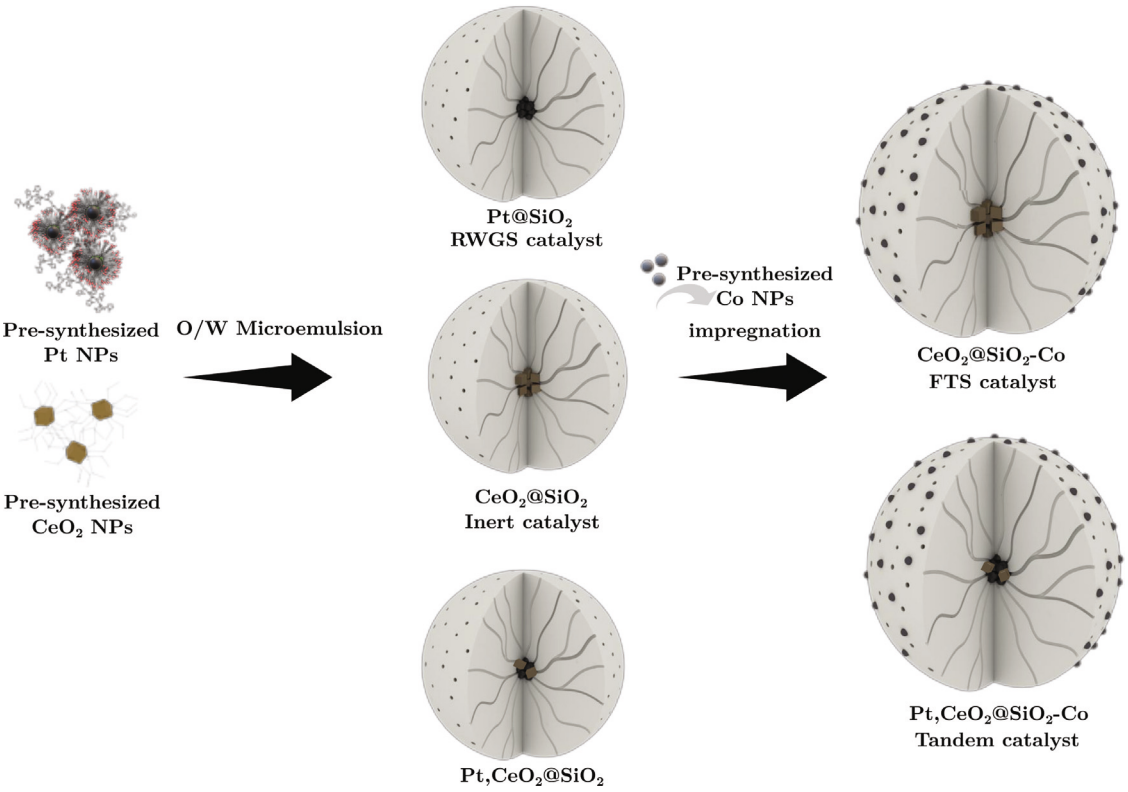

Fig. 1. Schematic overview of the steps for the rational synthesis of multi-core–shell catalysts; Step 1. synthesis of Pt and CeO_2 core NPs; Step 2. shell formation using O/W microemulsion method leading to Pt@SiO_2, RWGS catalyst, and CeO_2@SiO_2, inert catalyst, and Pt,CeO_2@SiO_2, core for tandem catalyst; Steps 3 and 4. synthesis of Co NPs and subsequent impregnation on to Pt,CeO_2@SiO_2 and CeO_2@SiO_2 resulting in CeO_2@SiO_2-Co, FTS catalyst, and Pt,CeO_2@SiO_2-Co, tandem catalyst.

the inert core in the tandem and FTS catalysts. The developed catalyst model addresses critical aspects of a tandem system, including the sequential arrangement of active metals enabled by the redispersion capability of pre-synthesized Pt and Co NPs in organic solvent. Additionally, proximity is achieved through the close distance between two active phases, approximately 75 nm apart, and compatibility is ensured by the ability to control the quantity of active metals situated on both the core and shell under the equilibrium conditions of synthesis.

To create an oil-in-water microemulsion system, initially, the core should be able to redisperse in an organic solvent, also good dispersibility is essential for further synthesis steps [39]. Here, oleic acid-capped CeO_2 NPs and PVP and TTAB-capped Pt NPs were easily redispersed in chloroform and used as an oil phase that solubilizes the oil domain into the nonpolar tail region of the surfactant to yield stable microstructure. The CeO_2 nuclei that were generated in water transferred into the toluene solution by using oleic acid as a stabilizing agent in the organic–inorganic interface, and polyhedral CeO_2 NPs with the size of 6.07 ± 0.10 nm have been formed through the oriented aggregation mechanism, Fig. S.2b. Mono disperse nanopolyhedra Pt NPs with the size of 3.11 ± 0.59 nm were obtained using one-pot polyol synthesis in which ethylene glycol was used as the reducing agent, PVP was used as the stabilizer and reducing agent, and TTAB as the capping agent, Fig. S.2a. The oleic and non-polar phases of Pt and Ce NPs undergo a phase transfer to the aqueous phase through a CTAB amphiphilic molecule [39]. Notably, Pt and Ce NPs are distributed in the core without aggregation or forming larger particles. Subsequently, a silica shell is coated onto Pt and Ce NPs through the hydrolysis and condensation of TEOS in the Stöber process, resulting in the formation of a mesoporous structure achieved by removing all templates, stabilizers, and surfactant molecules. Referring to the TEM images, Fig. S.2c–g, the formation of a well-defined core–shell structure consisting of multi-core NPs surrounded by a mesoporous silica shell is confirmed, also the presence of Co NPs distributed on the surface for tandem and FTS catalysts is revealed.

The average diameter of core–shell NPs and the distance between the external surface of the core and the surface of the shell are shown in Table 1. Also, this distance, named δ, varies with particle radius since the core NPs occupy a specific region within the nanoparticles. In particular, Pt,CeO_2@SiO_2-Co NPs exhibit a relatively larger diameter than δ, measuring approximately 205 nm and 69, respectively. This size discrepancy can be attributed to the unique composition of Pt and Ce as the core material, distinguishing it from other samples which feature only a single metal oxide in the core.

Fig. 2 shows STEM images of Pt,CeO_2@SiO_2-Co NPs. In the composition mode of secondary electron and backscattered electron image, Co NPs display a distinct bright contrast and are uniformly distributed on the surface of the silica shell. The EDS map suggests that Pt and Ce are concentrated in the center of the NPs, Simultaneously, Si and O are

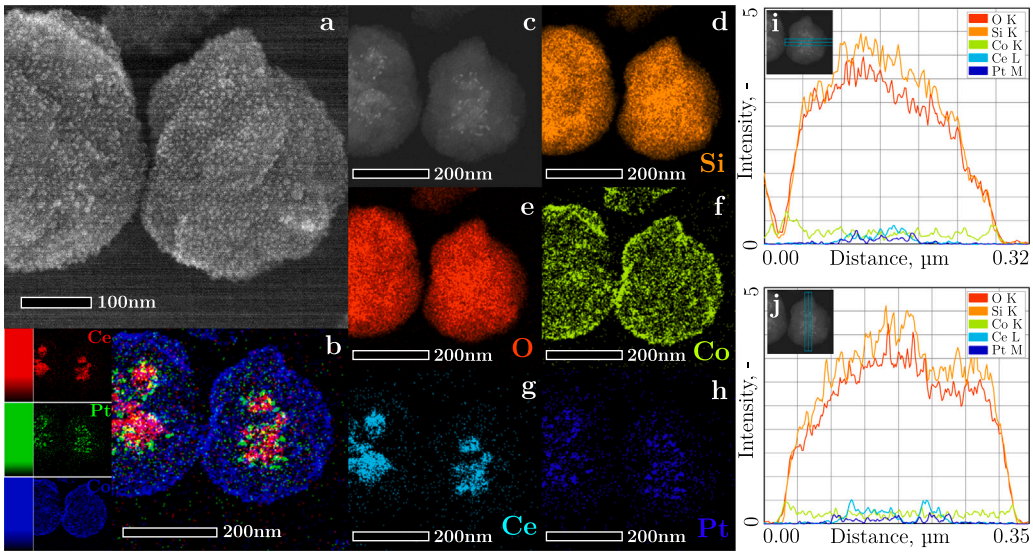

Fig. 2. Scanning Transmission Electron Microscopy (STEM) images of Pt,CeO_2@SiO_2-Co. (a) Secondary Electron and Backscattered Electron (SE/BSE), (b) Red-Green-Blue (RGB) overlay, (c) High-Angle Annular Dark-Field (HAADF); Energy-Dispersive X-ray Spectroscopy (EDS) elemental maps of (d) Si, (e) O, (f) Co, (g) Ce, (h) Pt; Line-scan profile of O, Si, Co, Ce, Pt and HAADF signals (i) Horizontal survey, (j) Vertical survey.

found to be uniformly distributed throughout the entire particle, i.e., a core–shell structure. On the basis of the EDS line profile of the NPs across the marked X and Y axes, in Fig. 2i–j, the detected intensity of Pt and Ce atoms increases from the particle's surface toward its core and proves that Pt and Ce NPs were mostly located as the core. Additionally, there is a correlated increase in the intensity of Si and O signals as the Co signal diminishes from the particle's surface toward the core. The element profiles are well in accordance with the etching XPS results, Fig. 3a.

Fig. 3a depicts the variations obtained in the Pt4f and Co2p spectra throughout the eleven levels of the etching process. The spectra of Ce3d, Si2p, and O1s are also shown in Fig. S.3. The Pt4f spectra are rendered undetectable at the surface, whereas the intensity of Pt increases with the etching level, providing evidence for the presence of Pt within the core. Conversely, the Co2p spectra exhibit a decremental trend with increasing etch levels, which the surface spectra displaying the highest intensity. Fig. 3c displays the fitting of the Pt4f spectrum corresponding to the 11th step of etching. The fitting of Pt4f was performed with three doublets in which the binding energy (BE) values of the $Pt4f_{7/2}$ peaks are at 71.81, 72.94, and 74.37 eV, accompanied by corresponding doublets for $Pt4f_{5/2}$ with a difference of 3.30 eV (+0.2 −0.1) [40–42]. It has been proposed that the peaks at 72.94 eV and 74.37 eV are associated with Pt oxidation states. This suggests the formation of PtO_x during the shell formation in the presence of ammonia and the subsequent calcination process. Because the oxidation state of Pt in Pt_3O_4 is lower than in PtO_2 and higher than in PtO, an intermediate BE is expected for Pt_3O_4 that is challenging to differentiate from PtO_2 [43]. However, α-PtO_2 has been identified as a thermodynamically stable structure on the Pt (111) surface under atmospheric oxygen pressure and low temperatures, while Pt_3O_4 is the stable oxide between 597–701 °C [44]. Consequently, we attributed the two doublets at 72.94 eV and 74.37 eV to PtO and PtO_2 species within the oxides present in our sample. The BE at 71.81 eV coincides with the 71.9 eV (±0.1) peak observed for metallic Pt and Pt bound to chemisorbed oxygen, as reported in Refs. [26,45], consistent with XRDs results.

Fig. 3b illustrates the Co2p spectra fittings for both the surface and the 11th step of etching. An slight increase in intensity on the low binding energy side of the $2p_{3/2}$ peak, along with increment in the intensity of satellite features of $2p_{3/2}$ during the etching, suggests alterations in the oxidation state of cobalt. For the high-resolution XPS spectra of $2p_{3/2}$, the surface exhibits five peaks, while the 11th etched level displays four peaks. The fitting of the spectra for Co^{2+} (780.7), Co^{3+} (779.3), and $Co^{\delta+}(0 > \delta > 2)$ and the corresponding satellites are shown in blue, purple, and orange, respectively [46]. Notably, the satellite peak centered at 789.8 eV is attributed to the shake-up excitation of Co^{3+}, while the peaks at 782.7 eV and 786.3 eV correspond to the satellite peaks of Co^{2+}. Analyzing the surface spectra fitting reveals the presence of Co^{2+} and Co^{3+}, indicating the phase of Co_3O_4 on the surface layer of cobalt. These fitting parameters align with those previously reported by Biesinger et al. [47]. The lower BE of Co^{3+} compared to Co^{2+} is attributed to the final relaxation state and Madelung potential. At the 11th level of etching, the shifts in lower BE and the appearance of a peak centered at 778 eV suggest the existence of reduced Co species. This observation combined with the disappearance of the Co^{3+} satellite implies that some Co_3O_4 overlayers may have been sputtered from the surface or possibly underwent direct reduction through exposure to argon ions. In addition to consideration of the BE values, satellite structures, and spin/orbit splitting, the interval between $Co2p_{3/2}$ and $Co2p_{1/2}$ is also used to determine the Co oxidation state species [48,49]. The energy level difference of 15 eV indicates that Co^{3+} is dominant, while the BE separation of 16.0 eV indicates an oxidation state of Co^{2+}. Overall, the predominant cobalt species on the surface layer is Co_3O_4, whereas, with etching, it shifts to CoO. For reference, the curve fitting parameters are provided in Table S.3.

X-ray diffraction (XRD) analysis was conducted to investigate the lattice structure of the NPs, and the results are shown in Fig. 3d. The broad diffraction peak observed at a 2θ ranging from 15 to 30 degrees is attributed to the amorphous silica structure, indicating the successful formation of amorphous silica during the shell synthesis process for all core–shell NPs. The distinctive peaks corresponding to the crystalline phase of cubic CeO_2 are clearly detectable in the inert, FTS, and tandem catalysts, all incorporating ceria in the core. For RWGS catalyst, peaks observed at 36.89 and 46.39 degrees align well with the (111) and (200) crystallographic planes of Pt. The peak detected at 36.45 degrees in both tandem and FTS catalysts corresponds to Co_3O_4, indicating that these samples share the same crystalline cobalt structure. Evidently, the tandem catalyst incorporates the active metals present in both FTS and RWGS catalysts at identical crystalline phases.

BET surface area was determined through N_2 sorption isotherm and BETSI (Table S.4, Fig. S.6–Fig. S.8). The catalysts present a combination of type IV and type II isotherms with a type H4 hysteresis loop. RWGS catalyst occupies the surface area of 611 $m^2\,g^{-1}$, whereas

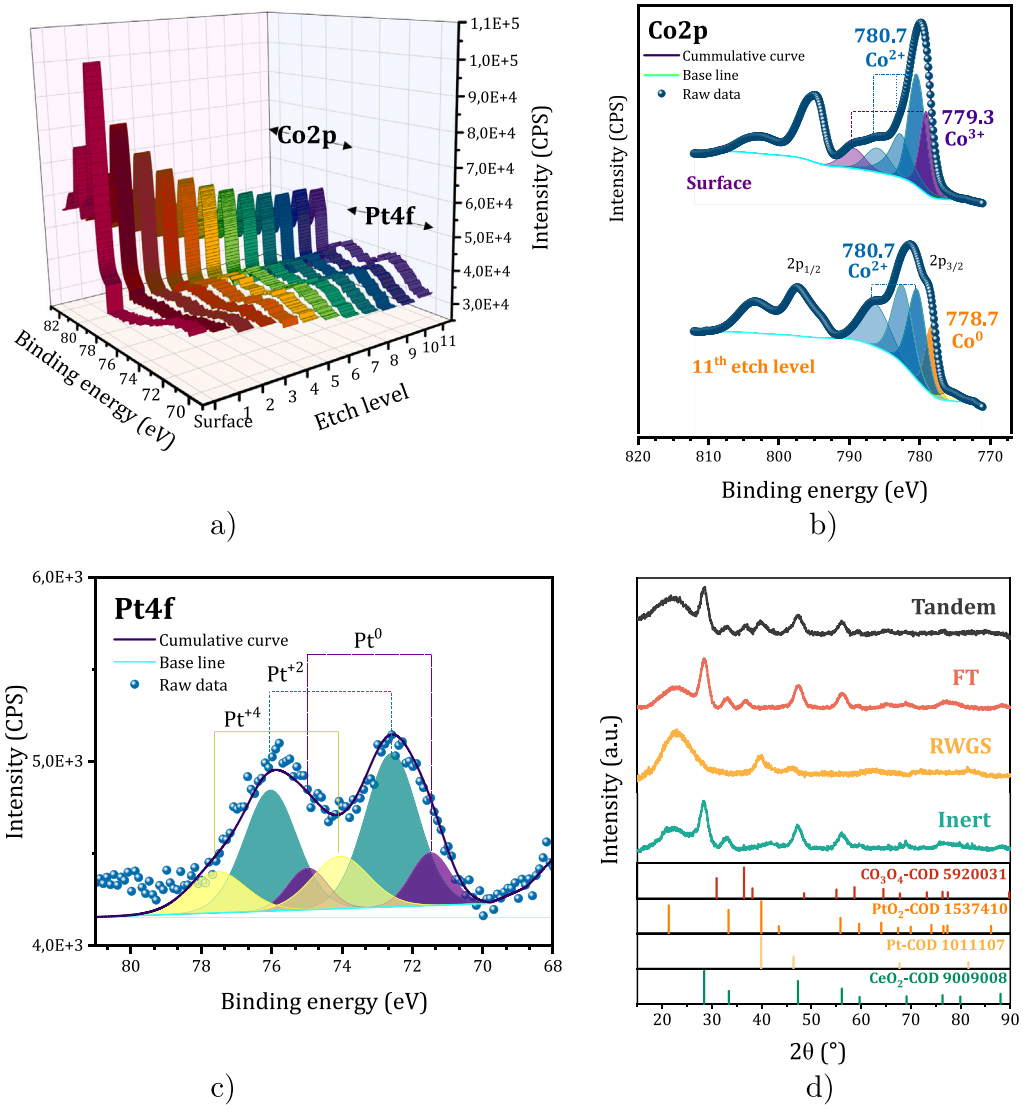

Fig. 3. XPS high-resolution spectra within Ar-etched of Pt,CeO_2@SiO_2-Co, (a) Pt4f and Co2P spectra during etching, (b) Co2P spectra at surface and 11th step of etching, (c) Pt4f spectra collected at 11th step of etching, and (d) Powder XRD patterns of calcined Inert, RWGS, FT, and Tandem catalysts.

FTS and tandem catalysts have surface areas of 298 and 219 $m^2\,g^{-1}$, respectively. This clearly illustrates a reduction in the specific surface area of the core–shell structure after the deposition of Co NPs on the outer shell layer, Fig. S.4. Pore size distribution, Fig. S.5, shows that catalysts have likely mesoporous structure and the distribution shifts toward larger pore size for FTS and tandem catalysts. The mean pore diameter measured 1.6 nm for RWGS, while it increased to 2.9 nm and 3.7 nm for FTS and tandem catalysts, respectively. This shift may be attributed to the potential blocking of smaller pores by Co NPs. Pore size and pore volume data are subsequently utilized in the calculations for determining the size of nanoparticles in the modeling section.

The investigation of CO_2 sorption revealed substantial uptakes even at room temperature for the RWGS, FTS, and tandem catalysts, Fig. S.9. The CO_2 sorption isotherms exhibited uptake values of 48, 18.5, and 21.5 $cm^3\,g^{-1}$ for the RWGS, FTS, and tandem catalysts, respectively. The higher CO_2 sorption observed in the RWGS catalyst suggests a stronger affinity of Pt for CO_2 sorption compared to Co, despite Co being more accessible and comprising almost ten times the weight percentage of Pt. However, the tandem catalyst exhibits lower sorption compared to the RWGS catalyst and higher sorption compared to the FTS catalyst. This observation underscores the accessibility of Pt NPs within the core, even in the presence of a silica shell and Cobalt coverage. It is important to note that a portion of the Pt NPs is hindered due to pore blockage.

The multi-metallic core–shell NPs were precisely synthesized to achieve the comparable weight percent of active metals among the catalysts. The Pt content in Pt@SiO_2 and Pt,CeO_2@SiO_2-Co are measured as 0.54 and 0.50 wt.%, while the Co amount in CeO_2@SiO_2-Co and Pt,CeO_2@SiO_2-Co are 4.72 wt.% and 3.86, respectively, cf. Table 1 [29]. Furthermore, the concentration of CeO_2 which acted as the inert core was found to be much lower than the other elements.

3.2. Catalytic test results and model comparison

Fig. 4 displays the carbon dioxide conversion over time on stream for inert, RWGS, FTS, and tandem catalysts under various operation conditions [29]. This plot highlights the increase in X.CO_2% for tandem catalyst compared to single-phase catalysts, providing evidence for the accessibility and activity of both active phases. CeO_2@SiO_2 which is considered as an inert catalyst showed activity of less than 1%. This low level of activity in comparison to other catalysts supports the assumption of its inert role. The results illustrate the greater stability of the Pt@SiO_2 compared to Pt,CeO_2@SiO_2-Co and CeO_2@SiO_2-Co, which indicates the protection function of the shell in sintering of NPs. The

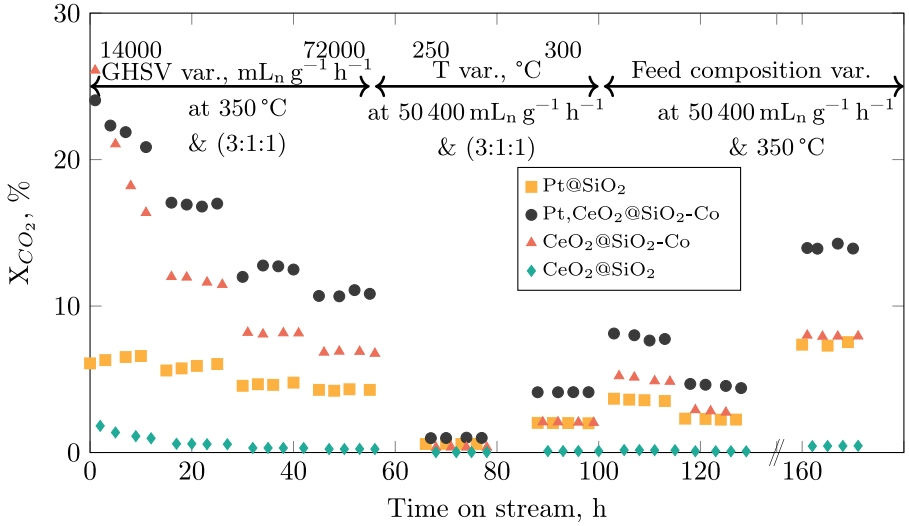

Fig. 4. CO_2 Conversion over time on stream for inert, RWGS, FTS, and tandem catalysts under various operation conditions.

observed decrease in activity for both tandem and FTS catalysts during the initial 20 h of the reaction can be attributed to the sintering of Co-NPs on the shell [21]. For all catalysts, the experimental X.CO_2% are less than X.CO_2% at thermodynamic equilibrium condition, Fig. S.14.

In Fig. 5, the results of the outgoing concentrations (molar fractions in %) from simulation and experiment for Pt,CeO_2@SiO_2-Co (tandem) are compared by means of parity plots. For a comparison in actual molar fractions please be referred to Fig. S.10. The dashed lines indicate a deviation of ±20%. The simulation was carried out with the estimated parameters of reactors 1 and 3 (cf. Table 3) and the design parameters according to Table 1. The concentrations of the educts CO_2 and H_2 at the reactor outlet are predicted very well by the model as Figs. 5(a) and 5(b) indicate. For the products CO and C_2H_6, the prediction is also good (cf. Figs. 5(c) and 5(e)), although the deviation increases towards lower overall values. The measured concentration of C_3H_8 is very low ($\leq 1e-3$%, near the detection limit) and the deviation seen in Fig. 5(f) can be explained with the gap of information from the mono-functional catalyst as stated in Section 2.6. The predictions of CH_4 tend to show a larger deviation between experiment and simulation as Fig. 5(d) indicates. From Table 3 it can be seen, that the standard deviation of the kinetic parameter $k_{7,1,0}$, which is responsible for the generation of C_{2+} alkanes, is large compared to the absolute value. Therefore, this parameter could not be estimated sufficiently with the experimental data at hand. The reason for that might be, that the adaptation from the original formulation reported in [34] was not successful, which might be due to either measurement error or a major impact of the support material on the reaction mechanism. Moreover, the assumption of super-positioning mono-functional kinetics to the tandem system cannot be validated by now. Nevertheless, Figs. S.10e and S.10f show qualitatively good agreement between simulation and experiment of the tandem system, which led to the conclusion that the modeling approach is suitable for the optimization. Generally, the product distribution is towards methane in hydrocarbon distribution. Experimental selectivity for CO, methane, and light hydrocarbons are plotted in Fig. S.11–Fig. S.13. RWGS catalyst demonstrates remarkably high selectivity for CO under different operation conditions. On the other hand, lower selectivity towards CO is observed for FTS and tandem catalysts, confirming that the FTS reactions also take place on the catalyst shell. It can be seen that higher C_{2+} selectivity is obtained for the tandem catalyst in comparison to both RWGS and FTS catalysts. Moreover, low GHSV and high temperature are in favor of C_{2+} production. Fig. S.15 shows methane as the main product in hydrocarbon distributions. It is to note that in this study, C_{2+} mainly consists of ethane.

Table 4
Results for catalyst loading and Yield of C_{2+} components from numerical optimization of tandem catalyst.

	y_{Pt} wt.%	y_{Co} wt.%	$Y_{C_{2+}}$ %
Experiment	0.5	3.8	0.26
Optimization $y_{inert} = 0.95$	1.76	3.24	0.36
Optimization $y_{inert} = 0.90$	3.36	6.63	0.61

3.3. Optimization of catalyst loading

Table 4 presents the results for the optimization of catalyst based on active metals loading on core and shell for experimental point No. 1 conditions (cf. Table S.1). By the optimization, the Yield for C_{2+} components was increased by (a) ≈38.5% and (b) ≈134.6%. In Fig. 6, the simulation results for all experimental conditions are depicted for the optimal and the experimental catalyst loading conditions. It can be seen, that for all reactor conditions, a significant increase in the Yield of C_{2+} components is achieved. In Table S.5, we have categorized the production of light hydrocarbon through CO_2 hydrogenation using core–shell structures in three general routes. Considering the 8.6 times higher amount of platinum in CeO_2-Pt@mSiO_2-Co [20] and three times higher amount of cobalt in SiO_2-Pt@m-SiO_2-Co [21] this system remains within the expected range of yield. Table 4 shows, that with increasing overall amount of active metal loading, the catalyst formulation used in this study gets closer to the ones reported in literature. It is crucial to consider the smaller distance between active metals located on the core and shell, i.e. the thickness of the shell, and other morphological differences in their designs that influence the Yield. Although the proposed synthesis approach is feasible in respect to controlling the ratio between the active phases it is important to mention the total yield of C_{2+} is less in such a tandem system in comparison to the methanol route as in [50].

4. Conclusion

In this article, we present a concise 5 step route for the design of optimal core–shell catalyst particles for tandem catalysis on the example of RWGS and FTS reactions. After initial thermodynamic calculations, the synthesis and the experimental characterization of the catalyst particles are shown. The catalyst particles are tested on their performance, individually and under tandem conditions in a parallel reactor setup to ensure consistent reaction conditions. Next to the

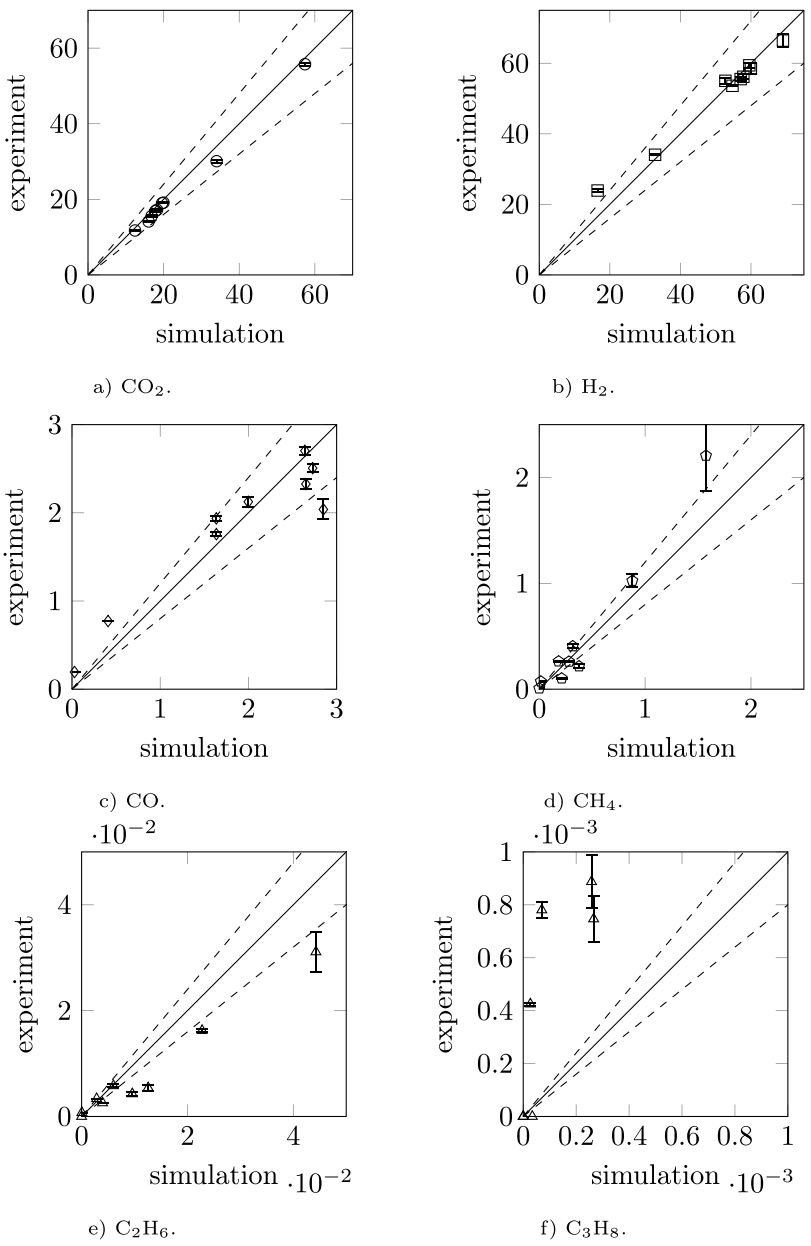

Fig. 5. Parity plots for molar fractions x (in %) from simulation and experiment for tandem catalyst Pt,CeO_2@SiO_2-Co; for (a) CO_2; (b) H_2; (c) CO; (d) CH_4; (e) C_2H_6; (f) C_3H_8 dashed lines indicate ±20%, the error bars stem from the standard deviation of the experimental results.

experimental investigation, a fast computing modeling approach [30] is adapted to the reaction system by using kinetics from literature. The kinetic parameters are estimated based on the mono-functional catalyst particle performance results and validated against the tandem catalyst configuration. The tuned model was then used for the numerical optimization of the catalyst design, i.e. catalyst loading for the maximization of C_{2+} Yield. It was shown that the catalyst performance could be increased significantly. The proposed method can be used as a blueprint for the design of optimal core–shell catalyst particles when promising candidates for the individual reactions are found and shall be combined for tandem catalysis. It is worth noting that the presented catalyst is generally probably not the best catalyst for the selected task as overall a maximum C_{2+} Yield of 0.61% is achieved. Nevertheless, only with the presented method its true potential could be assessed and evaluated and the same holds for other core–shell systems, as otherwise the degree of freedom for choosing the catalyst loading could not be eliminated from the performance tests.

CRediT authorship contribution statement

Najmeh Bashiri: Writing – original draft, Visualization, Investigation. **Georg Brösigke:** Writing – original draft, Investigation, Data curation, Conceptualization. **Esteban Gioria:** Writing – review & editing, Investigation, Data curation. **Johannes Schmidt:** Writing – review & editing, Investigation. **Martin Konrad:** Writing – review & editing, Data curation. **Rafael L. Oliveira:** Writing – review & editing, Validation, Investigation. **Michael Geske:** Writing – review & editing, Resources, Funding acquisition. **Frank Rosowski:** Writing – review & editing, Resources, Funding acquisition. **Sebastian Matera:** Writing – review & editing, Methodology. **Reinhard Schomäcker:** Writing – review & editing, Supervision, Resources, Funding acquisition. **Arne Thomas:** Writing – review & editing, Supervision, Resources, Project administration, Funding acquisition, Conceptualization. **Jens-Uwe Repke:** Writing – review & editing, Supervision, Resources, Project administration, Funding acquisition, Conceptualization.

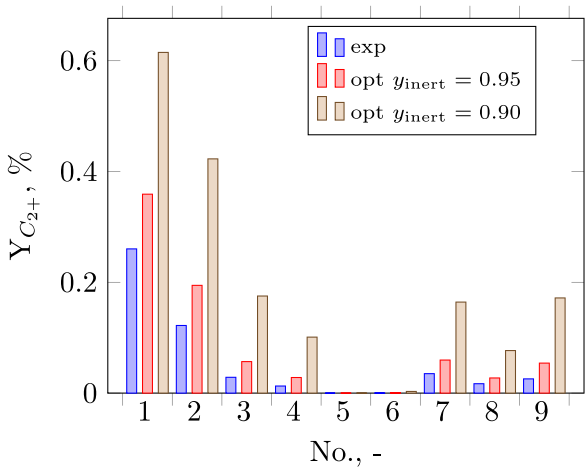

Fig. 6. Simulated Yields of accumulated C_{2+} components for tandem catalyst with catalyst loading from experimental catalyst setup (blue) and optimized catalyst with $y_{\text{inert}} = 0.95$ (red) and $y_{\text{inert}} = 0.90$ (brown).

Declaration of competing interest

The authors declare that they have no known competing financial interests or personal relationships that could have appeared to influence the work reported in this paper.

Data availability

Data will be made available on request.

Acknowledgments

Funded by the Deutsche Forschungsgemeinschaft (DFG, German Research Foundation) under Germany's Excellence Strategy – EXC 2008 – 390540038 – UniSysCat and project number 403371556 - GZ: INST 131/789-1 FUGG. We also acknowledge Sören Selve from ZELMI of TU Berlin for STEM support. Gefördert durch die Deutsche Forschungsgemeinschaft (DFG) im Rahmen der Exzellenzstrategie des Bundes und der Länder – EXC 2008/1 – 390540038 – UniSysCat.

Appendix A. Supplementary data

Supplementary material related to this article can be found online at https://doi.org/10.1016/j.cej.2024.153080.

References

[1] K.C. Nicolaou, T. Montagnon, S.A. Snyder, Tandem reactions, cascade sequences, and biomimetic strategies in total synthesis, Chem. Commun. 3 (2003) 551–564, http://dx.doi.org/10.1039/b209440c.

[2] D.J. Ramón, M. Yus, Asymmetric multicomponent reactions (AMCRs): The new frontier, Angew. Chem. Int. Edn 44 (2005) 1602–1634, http://dx.doi.org/10.1002/anie.200460548.

[3] F.X. Felpin, E. Fouquet, Heterogeneous multifunctional catalysts for tandem processes: An approach toward sustainability, 1, Wiley-VCH Verlag, 2008, pp. 718–724, http://dx.doi.org/10.1002/cssc.200800110,

[4] T.L. Lohr, T.J. Marks, Orthogonal tandem catalysis, Nature Chem. 7 (2015) 477–482, http://dx.doi.org/10.1038/nchem.2262.

[5] Y. Li, G. Yin, H. Guo, B. Zhou, A. Wu, One-pot synthesis of novel molecular clips and macrocyclic polyamines derived from bis(ethoxycarbonyl)glycoluril, Synthesis (2006) 2897–2902, http://dx.doi.org/10.1055/s-2006-942523.

[6] G. Yang, N. Tsubaki, J. Shamoto, Y. Yoneyama, Y. Zhang, Confinement effect and synergistic function of H-ZSM-5/Cu-ZnO-Al 2o3 capsule catalyst for one-step controlled synthesis, J. Am. Chem. Soc. 132 (2010) 8129–8136, http://dx.doi.org/10.1021/ja101882a.

[7] X.H. Gao, Q.X. Ma, T.S. Zhao, J. Bao, N. Tsubaki, Recent advances in multifunctional capsule catalysts in heterogeneous catalysis, 2018, http://dx.doi.org/10.1063/1674-0068/31/CJCP1805129.

[8] Y. Wang, H. Zhao, Tandem reactions combining biocatalysts and chemical catalysts for asymmetric synthesis, 2016, http://dx.doi.org/10.3390/catal6120194.

[9] N. Mota, E.M. Ordoñez, B. Pawelec, J.L.G. Fierro, R.M. Navarro, Direct synthesis of dimethyl ether from co2: Recent advances in bifunctional/hybrid catalytic systems, 2021, http://dx.doi.org/10.3390/catal11040411.

[10] J.C. Wasilke, S.J. Obrey, R.T. Baker, G.C. Bazan, Concurrent tandem catalysis, 2005, http://dx.doi.org/10.1021/cr020018n.

[11] G. Yin, B. Zhou, X. Meng, A. Wu, Y. Pan, Efficient C-C double-bond formation reaction via a new synthetic strategy: A self-sorting tandem reaction, Org. Lett. 8 (2006) 2245–2248, http://dx.doi.org/10.1021/ol060541e.

[12] M.J. Climent, A. Corma, S. Iborra, M.J. Sabater, Heterogeneous catalysis for tandem reactions, ACS Catal. 4 (2014) 870–891, http://dx.doi.org/10.1021/cs401052k.

[13] P. Li, Y. Yu, P.P. Huang, H. Liu, C.Y. Cao, W.G. Song, Core-shell structured MgAl-LDO@Al-MS hexagonal nanocomposite: An all inorganic acid-base bifunctional nanoreactor for one-pot cascade reactions, J. Mater. Chem. A 2 (2014) 339–344, http://dx.doi.org/10.1039/c3ta13403b.

[14] S. Zhang, Y. Hao, D. Su, V.V.T. Doan-Nguyen, Y. Wu, J. Li, S. Sun, C.B. Murray, Monodisperse core/shell Ni/FePt nanoparticles and their conversion to Ni/Pt to catalyze oxygen reduction, J. Am. Chem. Soc. 136 (2014) 15921–15924, http://dx.doi.org/10.1021/ja5099066.

[15] Y. Wei, S. Soh, M.M. Apodaca, J. Kim, B.A. Grzybowski, Sequential reactions directed by core/shell catalytic reactors, Small 6 (2010) 857–863, http://dx.doi.org/10.1002/smll.200902336.

[16] H. Yin, J. Choi, A.C. Yip, Anti-poisoning core-shell metal/ZIF-8 catalyst for selective alkene hydrogenation, Catal. Today 265 (2016) 203–209, http://dx.doi.org/10.1016/j.cattod.2015.08.030.

[17] L. Lin, T. Zhang, X. Zhang, H. Liu, K.L. Yeung, J. Qiu, New Pd/SiO2@ZIF-8 core-shell catalyst with selective, antipoisoning, and antileaching properties for the hydrogenation of alkenes, Ind. Eng. Chem. Res. 53 (2014) 10906–10913, http://dx.doi.org/10.1021/ie5013695.

[18] X. Lan, N. Huang, J. Wang, T. Wang, Geometric effect in the highly selective hydrogenation of 3-methylcrotonaldehyde over Pt@ZIF-8 core-shell catalysts, Catal. Sci. Technol. 7 (2017) 2601–2608, http://dx.doi.org/10.1039/c7cy00353f.

[19] J. Su, C. Xie, C. Chen, Y. Yu, G. Kennedy, G.A. Somorjai, P. Yang, Insights into the mechanism of tandem alkene hydroformylation over a nanostructured catalyst with multiple interfaces, J. Am. Chem. Soc. 138 (2016) 11568–11574, http://dx.doi.org/10.1021/jacs.6b03915.

[20] C. Xie, C. Chen, Y. Yu, J. Su, Y. Li, G.A. Somorjai, P. Yang, Tandem catalysis for CO2 hydrogenation to C2-C4 hydrocarbons, Nano Lett. 17 (2017) 3798–3802, http://dx.doi.org/10.1021/acs.nanolett.7b01139.

[21] E. Gioria, L. Duarte-Correa, N. Bashiri, W. Hetaba, R. Schomaecker, A. Thomas, Rational design of tandem catalysts using a core–shell structure approach, Nanoscale Adv. 3 (2021) 3454–3459, http://dx.doi.org/10.1039/D1NA00310K.

[22] S.K. Beaumont, S. Alayoglu, C. Specht, N. Kruse, G.A. Somorjai, A nanoscale demonstration of hydrogen atom spillover and surface diffusion across silica using the kinetics of CO2 methanation catalyzed on spatially separate Pt and Co nanoparticles, Nano Lett. 14 (2014) 4792–4796, http://dx.doi.org/10.1021/nl501969k.

[23] W. Li, H. Wang, X. Jiang, J. Zhu, Z. Liu, X. Guo, C. Song, A short review of recent advances in CO2 hydrogenation to hydrocarbons over heterogeneous catalysts, 2018, http://dx.doi.org/10.1039/c7ra13546g.

[24] Y.A. Daza, J.N. Kuhn, CO2 conversion by reverse water gas shift catalysis: Comparison of catalysts, mechanisms and their consequences for CO2 conversion to liquid fuels, RSC Adv. 6 (2016) 49675–49691, http://dx.doi.org/10.1039/c6ra05414e.

[25] S. Yang, L. Gao, Controlled synthesis and self-assembly of CeO2 nanocubes, J. Am. Chem. Soc. 128 (2006) 9330–9331, http://dx.doi.org/10.1021/ja063359h.

[26] C.K. Tsung, J.N. Kuhn, W. Huang, C. Aliaga, L.I. Hung, G.A. Somorjai, P. Yang, Sub-10 nm platinum nanocrystals with size and shape control: Catalytic study for ethylene and pyrrole hydrogenation, J. Am. Chem. Soc. 131 (2009) 5816–5822, http://dx.doi.org/10.1021/ja809936n.

[27] C. Liu, J. Guo, W. Yang, J. Hu, C. Wang, S. Fu, Magnetic mesoporous silica microspheres with thermo-sensitive polymer shell for controlled drug release, J. Mater. Chem. 19 (2009) 4764–4770, http://dx.doi.org/10.1039/b902985k.

[28] G. Greczynski, L. Hultman, X-ray photoelectron spectroscopy: Towards reliable binding energy referencing, Prog. Mater. Sci. 107 (2020) http://dx.doi.org/10.1016/j.pmatsci.2019.100591.

[29] N. Bashiri, M.R. Omidkhah, H.R. Godini, Study on carbon dioxide hydrogenation on olefin production over alumina supported catalysts, Thesis, Vol. 7, Tarbiat Modares University, 2022, pp. 136–138, URL: https://ganj.irandoc.ac.ir/#/articles/9ce5061a6e3c51b53f8cbb6239a0b0cc and https://www.researchgate.net/publication/380668495.

[30] G. Brösigke, J.-U. Repke, R. Schomäcker, S. Matera, The closer the better? Theoretical assessment of the impact of catalytic site separation for bifunctional core–shell catalyst particles, Chem. Eng. J. 446 (2022) 136891, http://dx.doi.org/10.1016/j.cej.2022.136891.

[31] V.A. Merchan, E. Esche, S. Fillinger, G. Tolksdorf, G. Wozny, Computer-aided process and plant development. a review of common software tools and methods and comparison against an integrated collaborative approach, Chem. Ing. Tech. 88 (1–2) (2015) 50–69, http://dx.doi.org/10.1002/cite.201500099.

[32] G. Tolksdorf, E. Esche, G. Wozny, J.-U. Repke, Customized code generation based on user specifications for simulation and optimization, Comput. Chem. Eng. 121 (2019) 670–684, http://dx.doi.org/10.1016/j.compchemeng.2018.12.006.

[33] O. Thinon, K. Rachedi, F. Diehl, P. Avenier, Y. Schuurman, Kinetics and mechanism of the water–gas shift reaction over platinum supported catalysts, Top Catal. 52 (13–20) (2009) 1940–1945, http://dx.doi.org/10.1007/s11244-009-9377-z.

[34] W. Qian, H. Zhang, W. Ying, D. Fang, The comprehensive kinetics of Fischer–Tropsch synthesis over a Co/AC catalyst on the basis of CO insertion mechanism, Chem. Eng. J. 228 (2013) 526–534, http://dx.doi.org/10.1016/j.cej.2013.05.039.

[35] B. Efron, Bootstrap methods: Another look at the jackknife, Ann. Statist. 7 (1) (1979) http://dx.doi.org/10.1214/aos/1176344552.

[36] E. Esche, C. Hoffmann, M. Illner, D. Müller, S. Fillinger, G. Tolksdorf, H. Bonart, G. Wozny, J.-U. Repke, MOSAIC - enabling large-scale equation-based flow sheet optimization, Chem. Ing. Tech. 89 (5) (2017) 620–635, http://dx.doi.org/10.1002/cite.201600114.

[37] R. Fourer, D.M. Gay, B.W. Kernighan, A modeling language for mathematical programming, Manage. Sci. 36 (5) (1990) 519–554, http://dx.doi.org/10.1287/mnsc.36.5.519.

[38] A. Wächter, L.T. Biegler, On the implementation of an interior-point filter line-search algorithm for large-scale nonlinear programming, Math. Program. 106 (1) (2005) 25–57, http://dx.doi.org/10.1007/s10107-004-0559-y.

[39] N.Q. Yin, P. Wu, T.H. Yang, M. Wang, Preparation and study of a mesoporous silica-coated Fe3O4 photothermal nanoprobe, RSC Adv. 7 (2017) 9123–9129, http://dx.doi.org/10.1039/c6ra28413b.

[40] J. Wang, G. Yin, Y. Shao, S. Zhang, Z. Wang, Y. Gao, Effect of carbon black support corrosion on the durability of Pt/C catalyst, J. Power Sources 171 (2007) 331–339, http://dx.doi.org/10.1016/j.jpowsour.2007.06.084.

[41] W. Huang, J.N. Kuhn, C.K. Tsung, Y. Zhang, S.E. Habas, P. Yang, G.A. Somorjai, Dendrimer templated synthesis of one nanometer rh and pt particles supported on mesoporous silica: Catalytic activity for ethylene and pyrrole hydrogenation, Nano Lett. 8 (2008) 2027–2034, http://dx.doi.org/10.1021/nl801325m.

[42] P.W. Seo, H.J. Choi, S.I. Hong, S.C. Hong, A study on the characteristics of CO oxidation at room temperature by metallic Pt, J. Hazard. Mater. 178 (2010) 917–925, http://dx.doi.org/10.1016/j.jhazmat.2010.02.025.

[43] L.K. Ono, J.R. Croy, H. Heinrich, B.R. Cuenya, Oxygen chemisorption, formation, and thermal stability of Pt oxides on Pt nanoparticles supported on SiO2/Si(001): size effects, J. Phys. Chem. C 115 (2011) 16856–16866, http://dx.doi.org/10.1021/jp204743q.

[44] N. Seriani, W. Pompe, L.C. Ciacchi, Catalytic oxidation activity of Pt3O4 surfaces and thin films, J. Phys. Chem. B 110 (2006) 14860–14869, http://dx.doi.org/10.1021/jp063281r.

[45] D.R. Butcher, M.E. Grass, Z. Zeng, F. Aksoy, H. Bluhm, W.X. Li, B.S. Mun, G.A. Somorjai, Z. Liu, In situ oxidation study of Pt(110) and its interaction with CO, J. Am. Chem. Soc. 133 (2011) 20319–20325, http://dx.doi.org/10.1021/ja207261s.

[46] X. Cao, D. Zhang, X. Cheng, Q. Xu, L. Zhang, L. Huang, Y. Tu, X. Yu, T. Zhang, Y. Li, H. Niemantsverdriet, J. Zhu, Adsorption and oxidation of CO on Co3O4/Ir(100) thin films, J. Phys. Chem. C 126 (51) (2022) 21638–21649, http://dx.doi.org/10.1021/acs.jpcc.2c07515.

[47] M.C. Biesinger, B.P. Payne, A.P. Grosvenor, L.W. Lau, A.R. Gerson, R.S.C. Smart, Resolving surface chemical states in XPS analysis of first row transition metals, oxides and hydroxides: Cr, Mn, Fe, Co and Ni, Appl. Surf. Sci. 257 (2011) 2717–2730, http://dx.doi.org/10.1016/j.apsusc.2010.10.051.

[48] C.-Y. Kwon, J.-Y. Jeong, J. Yang, Y.S. Park, J. Jeong, H. Park, Y. Kim, S.M. Choi, Effect of copper cobalt oxide composition on oxygen evolution electrocatalysts for anion exchange membrane water electrolysis, Front. Chem. 8 (2020) http://dx.doi.org/10.3389/fchem.2020.600908.

[49] M. Fantauzzi, F. Secci, M.S. Angotzi, C. Passiu, C. Cannas, A. Rossi, Nanostructured spinel cobalt ferrites: Fe and Co chemical state, cation distribution and size effects by X-ray photoelectron spectroscopy, RSC Adv. 9 (2019) 19171–19179, http://dx.doi.org/10.1039/c9ra03488a.

[50] J. Chen, X. Wang, D. Wu, J. Zhang, Q. Ma, X. Gao, X. Lai, H. Xia, S. Fan, T.-S. Zhao, Hydrogenation of CO2 to light olefins on CuZnZr@(Zn-)SAPO-34 catalysts: Strategy for product distribution, Fuel 239 (2019) 44–52, http://dx.doi.org/10.1016/j.fuel.2018.10.148.